



HAL
open science

Preparation and characterization of nanosized magnesium ferrite powders by a starch-gel process and corresponding ceramics

Roberto Köferstein, Till Walther, Dietrich Hesse, Stefan G Ebbinghaus

► To cite this version:

Roberto Köferstein, Till Walther, Dietrich Hesse, Stefan G Ebbinghaus. Preparation and characterization of nanosized magnesium ferrite powders by a starch-gel process and corresponding ceramics. *Journal of Materials Science*, 2013, 48 (19), pp.6509-6518. 10.1007/s10853-013-7447-x . hal-01995695

HAL Id: hal-01995695

<https://hal.science/hal-01995695>

Submitted on 27 Jan 2019

HAL is a multi-disciplinary open access archive for the deposit and dissemination of scientific research documents, whether they are published or not. The documents may come from teaching and research institutions in France or abroad, or from public or private research centers.

L'archive ouverte pluridisciplinaire **HAL**, est destinée au dépôt et à la diffusion de documents scientifiques de niveau recherche, publiés ou non, émanant des établissements d'enseignement et de recherche français ou étrangers, des laboratoires publics ou privés.

<http://link.springer.com/article/10.1007/s10853-013-7447-x>

**Preparation and characterization of nano-sized magnesium ferrite powders
by a starch-gel process and corresponding ceramics**

Roberto Köferstein^{a,*}, Till Walther^a, Dietrich Hesse^b, Stefan G. Ebbinghaus^a

^a*Institute of Chemistry, Inorganic Chemistry, Martin-Luther-University Halle-Wittenberg,
Kurt-Mothes-Strasse 2, 06120 Halle, Germany.*

^b*Max Planck Institute of Microstructure Physics, Weinberg 2, 06120 Halle, Germany.*

* Corresponding author. Tel.: +49-345-5525630; Fax: +49-345-5527028.
E-mail address: roberto.koefenstein@chemie.uni-halle.de

Abstract. The synthesis and characterization of nano-sized MgFe_2O_4 by a starch-gel method is described herein. A phase-pure nano-sized MgFe_2O_4 powder (**1a**) was obtained after calcining a (MgFe)-starch gel at 550 °C. The powder has a specific surface area of 60.6 m^2/g and a crystallite size of 9 nm. TEM investigations reveal particles in the range of 7 to 15 nm. The activation energy of the crystallite growth process was calculated as 89 ± 14 kJ/mol. The shrinkage and sintering behaviour of resulting compacts were studied. UV–VIS investigations of the nano-sized powder **1a** reveal an optical band gap of 2.38 eV, whereas calcination at 1100 °C (powder **1g**) leads to a crystallite size of 129 nm and a band gap of 2.16 eV. Magnetization loops at 300 K and the temperature dependence of both the field-cooled (FC)

and the zero-field-cooled (ZFC) magnetization indicate a superparamagnetic behaviour. The blocking temperature for powder **1a** was determined as 140 K at a field of $H = 500$ Oe. We found different saturation magnetizations (M_s) depending on the calcination temperature. Calcination at 550 °C (**1a**) results in $M_s = 20.0$ emu/g which increases with calcination temperature to a maximum of 37.7 emu/g for powder **1e** calcined at 900 °C. Ceramic bodies sintered between 1450 and 1600 °C exhibit M_s values of 25–28 emu/g. Magnetic investigations at 10 K on powders **1a–1g** show hysteresis loops with coercivities up to 950 Oe, remanences to 10 emu/g and M_s values to 50.4 emu/g. Additionally, the nano-scaled powders show a shift of the hysteresis loops.

Keywords: *soft-chemistry synthesis; sintering; magnetic properties; optical properties; spinel*

1. Introduction

Magnesium ferrite ($MgFe_2O_4$) is an important functional magnetic material which crystallizes in the spinel structure type. $MgFe_2O_4$ -based materials have found applications in microwave devices, computer memory chips and high-density recording media [1,2]. $MgFe_2O_4$ can also be used as catalyst for the oxidation of styrene [3], the dechlorination of polychlorinated aromatic compounds [4], and the decomposition of carbon particulates [5]. *Dom* et al. [6] investigated the photocatalytic activity and *Xiong* et al. [7] showed a catalytic effect of magnesium ferrite in a heterogeneous *Fenton*-like reaction.

Furthermore, $MgFe_2O_4$ finds application as gas- and humidity sensor [8,9], as semiconductor [10], and is also used as an inorganic pigment [11,12,13]. In addition it has been shown that $MgFe_2O_4$ is a promising candidate for local heat treatment in human cancer therapy [14,15]. *Okawa* et al. [16] used $MgFe_2O_4$ as cathode material in a molten carbonate fuel cell (MCFC). Moreover, composite materials consisting of $MgFe_2O_4$ and $BaTiO_3$ show multiferroic properties [17].

MgFe₂O₄ is a soft-magnetic n-type semiconducting material with a *Néel* temperature of around 400 °C [18,19]. The crystal structure lies between a normal spinel and an inverse spinel type and the fraction of tetrahedral sites occupied by Fe³⁺-ions depends on the temperature [18,19,20]. For this reason the chemical formula of magnesium ferrite can be written as ^T(Mg_{1-x}Fe_x)^O(Mg_xFe_{2-x})O₄, where T and O represent the tetrahedral and octahedral sites of the spinel-type structure, respectively. The inversion parameter *x* reflects the fraction of iron cations occupying the tetrahedral site [18,19].

To synthesise MgFe₂O₄ nanoparticles various chemical and physical approaches are reported such as high-energy ball milling [21], sol-gel [22], micelle [23,24], polymerization/co-precipitate [5,25,26] and combustion methods [27]. An electrospinning procedure was published by *Maensiri* et al. [28].

The aim of this paper is to describe a versatile and cheap one-pot synthesis route to obtain nano-sized MgFe₂O₄ by decomposition of a (MgFe)-gel using starch both as gellant and complexation agent. We have examined the decomposition process to MgFe₂O₄ via thermogravimetry (TG), mass spectroscopy (MS), and differential thermal analysis (DTA). Phase evolution and grain growth kinetics during the formation of MgFe₂O₄ have been investigated by X-ray powder diffraction (XRD). For the obtained powders of various particle sizes optical band gaps, magnetic properties, and the sintering behaviour yielding dense compacts have also been studied.

2. Experimental

2.1. Material preparation

Mg(NO₃)₂·6H₂O (0.006 mol, *Alfa Aesar*, >98 %) and Fe(NO₃)₃·9H₂O (0.012 mol, *Merck*, ACS) were dissolved in 15 ml water. 2 g soluble starch (*Sigma-Aldrich*, p.a) were added and the mixture was stirred on a heating plate for 15 min at room temperature. Afterwards the

temperature was raised to about 120–140 °C and the mixture was stirred and heated until it turned into a highly viscous red gel.

This (MgFe)-gel was calcined in static air at various temperatures for 2 h with a heating rate of 5 K/min to yield MgFe₂O₄ powders (**1a–1f**) with different particle sizes.

For comparative purposes, a coarse-grained MgFe₂O₄ powder (**2**) was prepared via the conventional mixed-oxide method. Stoichiometric amounts of Fe₂O₃ (*Sigma-Aldrich*, 99 %) and MgO (*Sigma-Aldrich*, 99 %) were well ground together in an agate mortar and fired at 1250 °C for 24 h in static air.

Tab. 1 summarizes the synthesis conditions of the MgFe₂O₄ powders.

For the sintering investigations, powder **1a** and **2** were mixed with 5 wt% of a saturated aqueous polyvinyl alcohol (PVA) solution as pressing aid and then the powders were pressed into pellets.

2.2. Characterization

X-ray powder diffraction patterns with a step size of $2\theta = 0.01^\circ$ were collected at room temperature on a *Bruker D8-Advanced* diffractometer, equipped with a one-dimensional silicon strip detector (LynxEye™) and operating with Cu-K_α radiation. Powder patterns were refined with the profile fitting software PowderCell [29]. Crystallite sizes were determined from the XRD line broadening using the *Scherrer* equation and the integral peak breadth (software suite WinXPOW [30]). The *Wilson*-equation was used to determine the strain parameter [30,31]. Dilatometric (shrinkage) investigations were performed in a flowing synthetic air atmosphere (50 ml/min) in a *Setaram* TMA 92-16.18 dilatometer. Simultaneous thermogravimetric (TG), mass spectrometry (MS) and differential thermoanalytic (DTA) measurements in flowing synthetic air (30 ml/min) were performed using a *Netzsch* STA 449

system equipped with a quadrupole mass spectrometer ESD 100 (*InProcess Instruments*). The thermoanalytic measurements of the decomposition of the (MgFe)-gel were carried out on a sample preheated at 200 °C for 1 h. The specific surface area (BET) was determined using nitrogen five-point gas-physisorption (Nova 1000, *Quantachrome Corporation*). The equivalent BET particle diameters were calculated assuming a spherical or cubic particle shape [32]. ATR-Fourier transformed infrared (FT-IR) spectra were collected at room temperature using a *Bruker Tensor 27* spectrometer equipped with a diamond ATR unit. Transmission electron microscopy (TEM) samples were prepared by dispersing the powder in alcohol under ultrasonic agitation, and collecting it onto a copper TEM grid covered with a carbon membrane. TEM images were recorded with a *Philips CM20Twin* at an electron energy of 200 keV. Scanning electron microscope images were recorded with a *Philips XL30 ESEM* (Environmental Scanning Electron Microscope). Diffuse reflectance spectra were obtained at room temperature in the range 380–1000 nm using a *Perkin Elmer UV–VIS* spectrometer Lambda 19. BaSO₄ was used as a white standard. Magnetic measurements were carried out using a PPMS 9 from *Quantum Design*. Hysteresis loops were taken at 300 K and 10 K with magnetic field cycling between –90 and +90 kOe. In addition, the temperature dependent magnetic moments were measured at H = 500 Oe in the temperature range of 5 to 300 K using field-cooled (FC) and zero-field cooled (ZFC) conditions.

3. Results and discussion

3.1. Thermal analysis

Heating of the (MgFe)-gel at 200 °C for 1 h in air resulted in a black-brown powder. Simultaneous TG-MS and DTA investigations up to 700 °C in flowing air (heating rate: 5 K/min) were carried out on this powder (Fig. 1a). We detected a weight loss of 7.5 % up to 250 °C by the evaporation of water from the surface, due to the hygroscopic nature of the sample. The DTA curve shows a very weak endothermic signal and the MS curve has a weak

signal for $m/z = 18$ (see inset in Fig. 1a). The strongly exothermic reaction between 285 and 319 °C is accompanied by a total weight loss of 49.2 %. This exothermic reaction is characterized by the evolution of CO_2 , H_2O , NO_2 , and NO and suggests a self-combustion like process in which the nitrate ions act as an oxidizing agent and the (partly decomposed) starch molecules as fuel. A proceeding second weaker exothermic process is finished at 408 °C. Simultaneous mass spectroscopy indicated the evaporation of small amounts of CO_2 , NO_2 , and NO . A very slight last weight loss is completed at about 600 °C and the total weight loss accounts to 56.8 %. XRD investigations on the final brown product indicated phase-pure cubic MgFe_2O_4 [33].

Fig. 1b shows TG/DTA measurements of the same powder as above but in argon atmosphere and up to 900 °C (heating rate: 5 K/min). Up to 500 °C we observed a weight loss of 51.3 %. XRD investigation of the black intermediate at 500 °C revealed weak reflections of FeO and elemental iron [33]. A last decomposition process between 570 and 830 °C led to a total weight loss of 64.0 %. The decomposition processes are accompanied by two endothermic signals. In contrast to the thermoanalytic measurements in air the decomposition in argon atmosphere results in a mixture of MgFe_2O_4 , $\text{Mg}_{1-x}\text{Fe}_x\text{O}$ [33] and elemental iron. The formation of both elemental iron and $\text{Mg}_{1-x}\text{Fe}_x\text{O}$ was also observed in the reduction of MgFe_2O_4 with H_2 [34]. The decomposition in argon atmosphere shows that atmospheric oxygen is essential for that combustion-like decomposition process to prepare phase-pure MgFe_2O_4 .

3.2. XRD, TEM, IR

Fig. 2 shows the phase evolution during the thermal decomposition of the red (MgFe)-gel. For these XRD investigations the samples of the (MgFe)-gel were heated in a muffle furnace in static air at various temperatures for 2 h (heating rate 5 K/min) resulting in fluffy powders. The as-prepared (MgFe)-gel is X-ray amorphous (Graph 2a). Up to a calcination temperature

of 400 °C we obtained only a weak and broad reflection around $2\theta \approx 35^\circ$ possibly due to the presence of Fe_2O_3 [33]. Broad reflections of pure cubic MgFe_2O_4 [33] appeared after a thermal treatment at 550 °C (Graph 2c). The resulting powder (**1a**) has a BET specific surface area of $60.6 \text{ m}^2/\text{g}$ corresponding to an equivalent particle size of 22 nm, which can be considered as the average size of the primary particles [35]. The volume-weighted average crystallite size (*Scherrer* equation) was calculated to be 9 nm. According to the Wilson-equation [31] the root-mean-square strain was found to be $5.5 \cdot 10^{-3}$ (see also Tab. 1). The calculated crystallite size is roughly by the factor two smaller than the size of the primary particles obtained from the BET data because the calcination procedure of the (MgFe)-gel leads to closely joined crystallites and surface areas unavailable for nitrogen adsorption [32]. TEM investigations (Fig. 3) of powder **1a** mainly show particles in the range of 7 to 15 nm as well as a small fraction of larger particles up to 20 nm. Graphs 2d and 2e exemplarily show XRD patterns of powders **1c** and **1f** calcined at 700 and 1100 °C, respectively. With higher calcination temperature the resulting powders show a decreasing specific surface area and increasingly crystallite sizes. The root-mean-square-strain is reduced with raising calcination temperature and is almost constant from 900 to 1100 °C (see Tab. 1).

The kinetics of crystallite growth can be expressed by the following phenomenological equation (1) [36]:

$$D^m - D_0^m = kt \cdot e^{-\frac{E_A}{RT}} \quad (1)$$

where D_0 is the initial crystallite size, D the crystallite size after calcination for the time t and at temperature T , k is the pre-exponential constant, m the crystallite growth exponent, E_A the activation energy for the crystallite growth process and R the universal gas constant.

The initial crystallite size D_0 is usually negligibly small, therefore equation 1 can be simplified to:

$$D^m = kt \cdot e^{\frac{-E_A}{RT}} \quad (2)$$

The kinetic crystallite growth exponent m can be determined from the inverse slope of $\ln D$ vs. $\ln t$. For that purpose we estimated the crystallite sizes after calcining the (MgFe)-gel at 600 °C for different times from 2 h up to 100 h. From Fig. 4a the crystallite growth exponent was found to be $m = 7.7$. The activation energy of the crystallite growth process during the calcination can be calculated from the slope of an Arrhenius plot ($\ln D^{7.7}/t$ vs. $1/T$) as shown in Fig. 4b. It was calculated as $E_A = 89 \pm 14$ kJ/mol.

Fig. 5 represents FT-IR spectra (ATR technique) of the (MgFe)-gel, corresponding calcination products at 550 °C (powder **1a**) and 1000 °C (powder **1f**). The broad band between about 3700 and 2600 cm^{-1} in the spectrum of the (MgFe)-gel (Graph 5a) is caused by O–H stretching and C–H stretching vibrations from water and starch molecules [37]. The O–H bending mode is reflected by an absorption band at 1635 cm^{-1} [38]. Anti-symmetric and symmetric N–O vibrations from NO_3^- ions appear at 1339 cm^{-1} and as a shoulder at 1042 cm^{-1} [38]. The additional shoulder at 1406 cm^{-1} represents O–C–H, C–C–H, and C–O–H bending modes from the starch [37]. C–O–H groups cause C–O stretching vibrations at 1152 cm^{-1} , whereas C–O stretching modes from C–O–C groups appear at 1080 and 1022 cm^{-1} [39].

The IR spectra of powder **1a** and **1f** show two characteristic adsorption bands ν_1 and ν_2 (Graph 5b,c) The higher frequency band (ν_1), which appears at 539 (**1a**) and 536 cm^{-1} (**1f**) can be assigned to an iron–oxygen stretching vibration on the tetrahedral site. The lower frequency band (ν_2) at 395 (**1a**) and 402 cm^{-1} (**1f**) is caused by the iron–oxygen stretching vibration on the octahedral site [40]. According to *Josyulu* and *Sobhanadri* [41] the weak absorption band at around 350 and 360 cm^{-1} (ν_3) stems from a magnesium–oxygen stretching vibration on the octahedral site.

The XRD patterns of the nano-powder **1a** was refined on the basis of a cubic unit cell (space group: Fd-3m) [42] and the cell parameter was calculated as $a = 838.40$ pm, which corresponds well to previously reported data for MgFe_2O_4 [18,42].

3.3. Sintering behaviour and microstructure

Fig. 6 shows the non-isothermal dilatometric investigations up to 1550 °C in flowing air (heating rate: 10 K/min). Since the green compacts **1a** (2.0 g/cm³) and **2** (3.3 g/cm³) strongly differ in their densities the values of the relative shrinkage are not directly comparable. Therefore, from the relative shrinkages the evolution of the relative densities was calculated assuming an isotropic behaviour of the compacts.

The shrinkage behaviour of compact **1a** reveals a distinctive two-step characteristic. A first shrinkage process starts at about 610 °C and has a maximum of the shrinkage rate of -0.86 %/min at 820 °C. The second step begins at 1150 °C and shows a shrinkage rate maximum at 1323 (-0.28 %/min). The first step accounts to about 60 % of the total shrinkage. The rates of both shrinkage steps are more than 0.1 %/min indicating sliding processes (viscous flow) as dominant shrinkage mechanism, primarily caused by the nano particles [43,44]. Between the two shrinkage steps there is a plateau at about 950 – 1150 °C where the shrinkage is very small. According to investigations of *Hirata* et al. [45] we assume that this stage is dominated by grain growth within secondary particles (agglomerate) in such a way that almost no pores are eliminated. The final calculated relative density reaches 85 % at 1550 °C.

For comparison purposes we also investigated a coarse-grained MgFe_2O_4 powder (**2**). That powder (Graph 2f) results from a conventional mixed-oxide synthesis at 1250 °C for 24 h and has a specific surface area of 1.1 m²/g and an equivalent particle size of 1215 nm.

The shrinkage of compact **2** starts at approximately 1150 °C and a small shrinkage rate maximum of -0.09 %/min appears at 1185 °C. At about 1380 °C the slope of the shrinkage curve changes, indicating a second shrinkage step, which is not yet finished up to 1550 °C.

The sample reaches a final relative density of 80 %. Since the low shrinkage rate of compact **2** is about 0.1 %, sliding processes play no important role during the sintering. Hence diffusion processes are more relevant during the densification of the micrometer-sized compact **2** than in the nano-particular compact **1a** [44].

The final bulk densities of ceramic bodies of **1a** after isothermal sintering at various temperatures with a soaking time of 1 and 10 h, respectively, are shown in Fig. 7. The bulk densities of the sintered bodies were calculated from their weight and geometric dimensions. The relative bulk densities (r.d.) of the ceramic bodies refer to the crystallographic density of 4.49 g/cm^3 [46]. After a soaking time of 1 h we obtain ceramic bodies with a relative density of 84 % at $1450 \text{ }^\circ\text{C}$ (grain size: 3–15 μm , Fig. 8a) and 88 % at $1500 \text{ }^\circ\text{C}$ (grain size: 3.5–15 μm). Dense ceramic bodies (relative density $\geq 90 \%$) form only at a sintering temperature of $1550 \text{ }^\circ\text{C}$ (90 %, grain size: 6–18 μm) and a relative density of 94 % is found at $1600 \text{ }^\circ\text{C}$ (grain size: 6–25 μm). However, a prolonged soaking time of 10 h leads to dense ceramic bodies even at $1450 \text{ }^\circ\text{C}$ (91 %, grain size: 4–28 μm , Fig. 8b). At $1500 \text{ }^\circ\text{C}$ and $1550 \text{ }^\circ\text{C}$ the relative densities are raised to 93 and 96 % and the grain sizes are in the range of 5–42 and 16–50 μm , respectively. EDX analysis on the surface of a compact sintered for 10 h at $1550 \text{ }^\circ\text{C}$ reveal some grains consisting of MgO. The XRD pattern (not shown) of that ceramic shows reflections of cubic MgFe_2O_4 and traces of MgO. These results are consistent with investigations reported by *Phillips et al.* [47]. They found in samples after equilibration at $\geq 1500 \text{ }^\circ\text{C}$ besides the main phase MgFe_2O_4 the secondary MgO phase. *Ahmed et al.* [48] sintered a conventional mixed-oxide MgFe_2O_4 powder at $1550 \text{ }^\circ\text{C}$ for 2 h and obtained a ceramic body with a density of 3.71 g/cm^3 (83 %).

From these experiments it is evident that the nano-crystalline MgFe_2O_4 prepared from the decomposition of the starch precursor shows improved sintering properties, which is

advantageous for all applications that require dense ceramics, such as in microwave devices [1,49].

3.4 Magnetic measurements

Table 2 summarizes the magnetic data of the MgFe_2O_4 powders **1a–1g**. The evolution of magnetization (M) depending on the applied field (H) at 300 K is demonstrated in Fig. 9 for powders **1a**, **1c**, **1e** and **1g**. The saturation magnetization (M_s) was evaluated by extrapolation of the magnetization *versus* $1/H$ to $1/H \rightarrow 0$, according to the *Law of Approach to Saturation* [50]. Magnetic measurements at 300 K reveal a saturation magnetization for sample **1a** of $M_s = 20.0$ emu/g, which increases with increasing crystallite size and/or calcination temperature and reaches a maximum of $M_s = 37.7$ emu/g at 900 °C. Further calcinations at 1000 and 1100 °C and thus increasing crystallite sizes cause a gradual reduction of M_s (inset in Fig. 9). It is well known that among other things M_s is influenced by the crystallite size, the inversion parameter (x), and surface effects (i.e. spin-glass like behaviour of the surface spins) [23,51]. With increasing particle size, surface effects are gradually reduced. Therefore the reduction of M_s from crystallite sizes above 60 nm (powder **1f**, **1g**) is possibly dominated by an increase of x [51,52].

The coercivity (H_c) and remanence (M_r) values for sample **1a** and **1b** are very small indicating a superparamagnetic behaviour [23] in accordance with the observed small crystallite sizes. The calculated M_r/M_s ratios for all samples are lower than 0.1 indicating an appreciable fraction of superparamagnetic particles at 300 K [53]. Fig. 10 exemplarily shows the temperature dependence of the magnetization under zero-field-cooled (ZFC) and field-cooled (FC) conditions with an external field of 500 Oe for powder **1a**. The magnetization of the FC curve decreases with increasing temperature, while the ZFC curve increases as temperature is increased up to a maximum corresponding to the blocking temperature (T_B). Above the blocking temperature the ZFC curve starts to decrease. The formation of a maximum in the

ZFC curve is a result of the superparamagnetic behaviour of the sample [54]. T_B increases with the crystallite size from 140 K for powder **1a** ($d_{\text{cryst}} = 9$ nm) to 210 K for powder **1c** ($d_{\text{cryst}} = 13$ nm). *Chen and Zhan* [55] determined a blocking temperature for MgFe_2O_4 nanoparticles (11 nm) of about 170 K, in good accordance with values found in this work.

Below the blocking temperature the field dependent magnetization of the MgFe_2O_4 powders show the formation of pronounced hysteresis loops. Fig. 11 shows M–H loops at 10 K for powders **1a**, **1c**, **1e**, and **1g**, exemplarily. Values of the coercivity between 950 and 60 Oe and remanences between 10.3 and 5.0 emu/g were found, indicating a ferromagnetic behaviour (inset I in Fig. 11). M_s values at 10 K are in the range from 28.3 to 50.4 emu/g, whereas the dependence of M_s on the crystallite size is analogous to the measurements at 300 K (inset II in Fig. 11). Closer inspection shows a small shift (ΔH_c) of the hysteresis loops (exchange bias-like) at 10 K of the nano-scaled MgFe_2O_4 powders (Tab. 2) in the negative direction, therefore we found different coercivity values for decreasing and increasing field as demonstrated for powder **1a** in Fig. 12. Based on *Nogues and Schuller* [56] the coercivity shift is defined as $\Delta H_c = |0.5(H_{c(\text{df})} + H_{c(\text{if})})|$, where $H_{c(\text{df})}$ is the coercivity at decreasing field and $H_{c(\text{if})}$ is the coercivity at increasing field. ΔH_c describes the shift of the centre (half width) of the hysteresis loop with respect to the origin ($H = 0$). Powder **1a** with $d_{\text{cryst}} = 8$ nm has a loop shift of $\Delta H_c = 81$ Oe, which decreases with increasing crystallite size (inset in Fig. 12). Loop shifts between 60–200 Oe were also found in high-energy milled nanocrystalline MgFe_2O_4 [52,57,58]. Loop shifts occur in materials with ferromagnetic/anti-ferromagnetic interfaces (exchange bias) [56]. Calculations on spherical NiO nano-particles by *Kodama et al.* [59] showed that the loop shift originates from the interaction between the reduced coordinated surface spins and the core. According to the core-shell model by *Sepelak et al.* [57] we can assume that the nanocrystalline MgFe_2O_4 consist of a ferrimagnetic core and a surface (grain

boundary) with uncompensated spins. The exchange coupling between the core and the shell leads to the observed loop shift.

M–H loops at 300 K of ceramic bodies sintered at 1450 °C for 1 h (grain size: 3–15 µm) reveal a M_s value of 28.2 emu/g, which only slightly decreases to about 26 emu/g after sintering at ≥ 1500 °C (Fig. 13, Tab. 3). Sintering for 10 h leads to the same tendency. Measurements at 10 K reveal saturation magnetizations between 32.7 and 35.9 emu/g. Coercivity and remanence of the ceramic bodies do not differ significantly from zero and indicated a blocking temperature above 300 K.

The coarse-grained powder **2** has a saturation magnetization of 28.2 emu/g at 300 K and 32.6 emu/g at 10 K and its magnetic behaviour is similar to the ceramic bodies described above. The saturation magnetizations both for the ceramic bodies and powder **2** are in good agreement with the reported M_s value of 33 emu/g at 3 K for bulk $MgFe_2O_4$ [57].

3.5. Diffuse reflectance measurements

Reported band gaps for $MgFe_2O_4$ samples are in the range of 2.0–2.2 eV [10,60,61]. To determine the optical band gap of $MgFe_2O_4$ diffuse reflectance spectra were recorded in the range of 380 to 1000 nm, as demonstrated in Fig. 14. The samples show a high reflectance in the visible range. The *Kubelka–Munk* theory was used for the analysis of diffuse reflectance spectra as expressed by the following equation [62,63]:

$$F(R) = \frac{(1-R)^2}{2R} \quad (4)$$

where $F(R)$ is the *Kubelka–Munk* function and R the reflectance.

The optical band gap can be determined according to equation 5 [64]:

$$\alpha h\nu = k(h\nu - E_g)^{1/n} \quad (5)$$

where α is the absorption coefficient, which is proportional to $F(R)$, k is an energy-independent constant, E_g the optical band gap. The exponent n is determined by the type of transition: $n = 2$ for direct allowed transitions, $n = 2/3$ for direct forbidden transitions, $n = 1/2$ for indirect allowed transitions and $n = 1/3$ for indirect forbidden transitions.

The *McLean* analysis [64,65] of the absorptions edge was applied to determine the exponent n and thus the type of transition. In the range of the absorption edge $(F(R) \cdot h\nu)^n$ vs. $h\nu$ should give a straight line. We found the best choice was $n = 2$ for all samples indicating that the direct allowed transition is dominant in the samples. Hence equation 5 can be written as:

$$F(R) \cdot h\nu = k(h\nu - E_g)^{1/2} \quad (6)$$

The optical band gap (E_g) can be determined by plotting $(F(R) \cdot h\nu)^2$ vs. $h\nu$ and extrapolating the slope to $F(R) \rightarrow 0$ as exemplarily shown in the inset in Fig. 14.

For powder **1a** (calcination at 550 °C) an optical band gap of 2.38 ± 0.05 eV was found, whereas calcination at 1100 °C (powder **1g**) lead to a reduction of the band gap to 2.16 ± 0.02 eV. The reduction is probably a result of the crystallite-/particle growth [66] (see also Tab. 1). The band gap energies of ceramic bodies sintered at 1450 °C and 1550 °C (soaking time 1 h) do not significantly differ from each other and reveal slightly lower values of 2.11 ± 0.02 eV and 2.10 ± 0.02 eV, respectively. On the other hand the coarse-grained mixed-oxide powder **2** has a band gap of 1.91 ± 0.01 eV. The variation of the band gap with increasing particle size is an important aspect for photocatalytic applications of MgFe_2O_4 [6].

Conclusion

We prepared nano-sized MgFe_2O_4 powders by decomposition of a (MgFe)-gel obtained using starch as a gellant and complexation agent. Calcining in air of the (MgFe)-gel at $550\text{ }^\circ\text{C}$ leads to a nano-crystalline powder (**1a**) with crystallite sizes of 9 nm. TEM images show particles in the range of 7–15 nm. The crystallite size increases to 116 nm by calcining at $1100\text{ }^\circ\text{C}$. The activation energy for crystallite growth was found to be $89 \pm 14\text{ kJ/mol}$. Dilatometric measurements of compacts of **1a** show a distinctive two-step behaviour of the densification. The shrinkage starts at about $610\text{ }^\circ\text{C}$. Dense ceramic bodies with relative densities $\geq 90\%$ can be obtained after isothermal sintering at $1550\text{ }^\circ\text{C}$ for 1 h and $1450\text{ }^\circ\text{C}$ for 10 h, respectively. On the basis of diffuse reflectance spectra the optical band gap of MgFe_2O_4 calcined at $550\text{ }^\circ\text{C}$ (**1a**) was determined as 2.38 eV and was found to decrease with raising calcination temperature and in turn increasing particle size to 2.16 eV (calcination at $1100\text{ }^\circ\text{C}$, **1d**). Ceramic bodies reveal optical band gaps at 2.1 eV.

Powder **1a** shows a saturation magnetization of 20 emu/g at 300 K. Increasing calcination temperatures to $900\text{ }^\circ\text{C}$ cause a raising saturation magnetization up to 37.7 emu/g, whereas M–H loops at 10 K reveal saturation magnetization up to 50 emu/g. We found a small shift (exchange bias) of the hysteresis loops depending on the crystallite size at 10 K. The MgFe_2O_4 nano-sized samples show a typical superparamagnetic behaviour. They show the formation of hysteresis loops below the blocking temperature, whereas above the blocking temperature the hysteresis behaviour disappeared.

The saturation magnetization at 300 K of the obtained ceramic bodies varies only slightly with temperature and soaking time and lies between 25 and 28 emu/g.

The MgFe_2O_4 powders show different magnetic properties depending on their particle sizes. This offers the possibility to modify the magnetoelectric coupling phenomena in multiferroic

composites. Additionally, the superparamagnetic samples are potential candidates for applications as ferrofluid or contrast medium in the magnetic resonance tomography.

Acknowledgements

The authors thank Dr. Th. Müller for TG/MS-DTA and Dr. L. Jäger for UV-VIS measurements. Financial support by the German Science Foundation within the Collaborative Research Centre (SFB 762) “Functionality of Oxide Interfaces” is gratefully acknowledged.

Table 1

BET surface area, particle-/crystallite size and root-mean-square-strain (ϵ) of MgFe_2O_4 powders

| Sample | Calcination procedure | S_{BET} (m^2/g) | d_{BET} (nm) ¹⁾ | d_{cryst} (nm) ²⁾ | ϵ ($\times 10^3$) |
|-----------|-----------------------|--|--|--|------------------------------|
| 1a | 550 °C/ 2h | 60.6 | 22 | 9 | 5.5 |
| 1b | 600 °C/ 2h | 39.6 | 34 | 11 | 3.9 |
| 1c | 700 °C/ 2h | 19.1 | 70 | 13 | 3.4 |
| 1d | 800 °C/ 2h | 6.0 | 223 | 32 | 1.3 |
| 1e | 900 °C/ 2h | 3.2 | 418 | 57 | 0.8 |
| 1f | 1000 °C/ 2h | 2.6 | 514 | 86 | 0.8 |
| 1g | 1100 °C/ 2h | 2.3 | 573 | 129 | 0.8 |
| 2 | 1250°C/ 24h | 1.1 | 1215 | - | - |

1) calculated from the specific surface area

2) volume-weighted average crystallite size (Scherrer equation)

Table 2

Saturation magnetization (M_s), coercivity (H_c) and remanence (M_r) of synthesized MgFe_2O_4 powders at 300 K and 10 K

| Sample | M_s (emu/g) | | H_c (Oe) | | ΔH_c (Oe) ²⁾ | M_r (emu/g) | |
|--------|---------------|------|------------|--------------------|---------------------------------|---------------|--------------------|
| | 300 K | 10 K | 300 K | 10 K ¹⁾ | | 300 K | 10 K ¹⁾ |
| | | | | | | | |

| | | | | | | | |
|-----------|------|------|------|-----|-----|-----|-----|
| 1a | 20.0 | 28.3 | ~0 | 950 | 81 | ~0 | 6.6 |
| 1b | 23.0 | 31.8 | ~0 | 671 | 67 | ~0 | 7.5 |
| 1c | 28.3 | 38.4 | 15.2 | 390 | 33 | 0.4 | 9.7 |
| 1d | 35.5 | 47.4 | 67.2 | 220 | 11 | 3.0 | 9.5 |
| 1e | 37.7 | 50.4 | 56.6 | 146 | 3.5 | 2.8 | 7.9 |
| 1f | 36.9 | 49.5 | 63.4 | 143 | 3 | 2.9 | 7.5 |
| 1g | 33.9 | 48.6 | 10.5 | 62 | 1 | 0.6 | 5.2 |

¹⁾ H_c and M_r (absolute values) were determined from the decreasing field

²⁾ calculated from $\Delta H_c = |0.5(H_{c(df)} + H_{c(if)})|$

Table 3

Saturation magnetization (M_s) of ceramic bodies from powder **1a** at 300 K and 10 K

| Sintering condition | Grain-size range (μm) | M_s (emu/g) | |
|---------------------|------------------------------------|---------------|------|
| | | 300 K | 10 K |
| 1450 °C/ 1h | 3–15 | 28.2 | 35.9 |
| 1500 °C/ 1h | 3.5–15 | 26.5 | 33.5 |
| 1550 °C/ 1h | 6–18 | 25.9 | 32.7 |
| 1600 °C/ 1h | 6–25 | 26.6 | 33.4 |
| 1450 °C/ 10h | 4–28 | 27.3 | 34.5 |
| 1500 °C/ 10h | 5–42 | 25.3 | 31.8 |
| 1550 °C/ 10h | 16–50 | 26.0 | 32.7 |

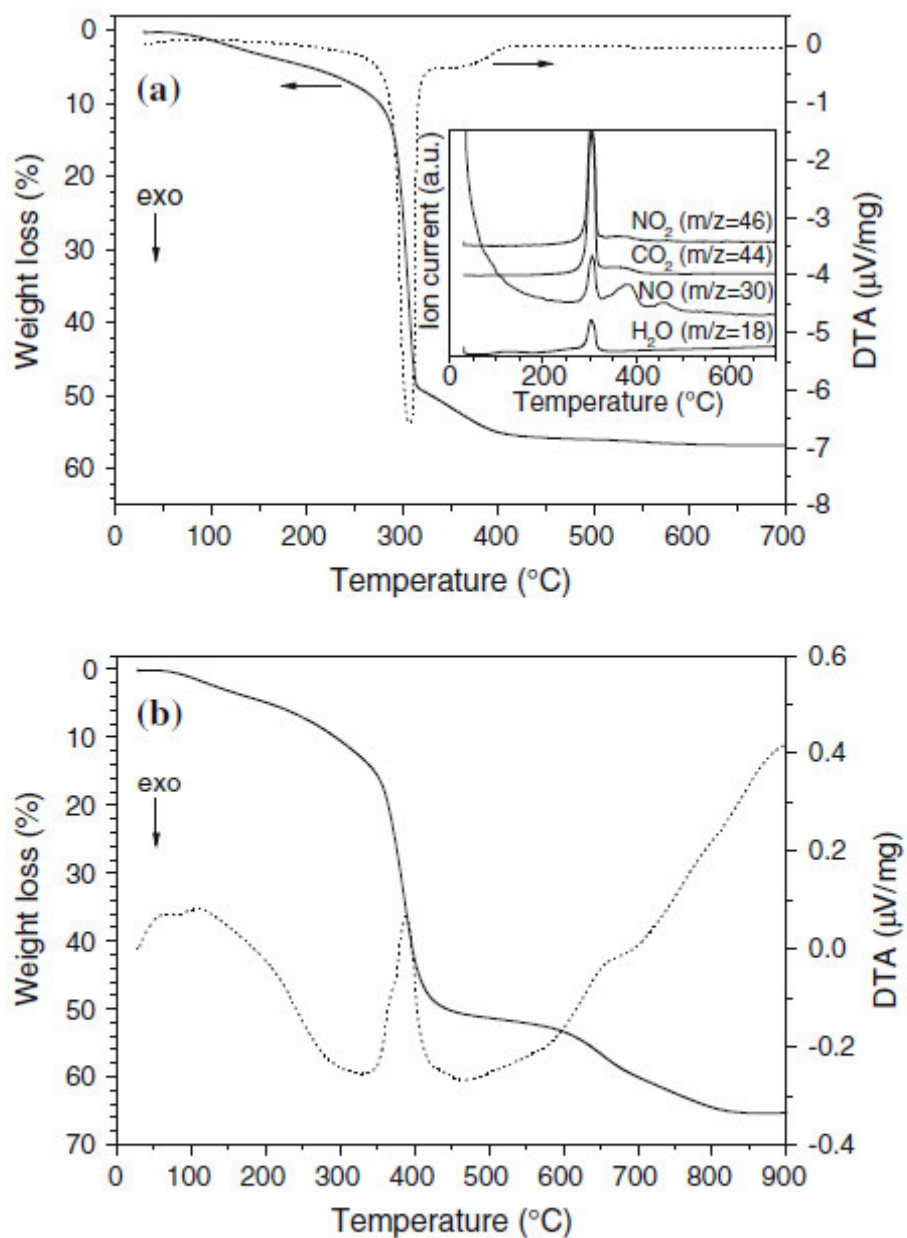


Fig. 1 Simultaneous TG-MS and DTA investigations (heating rate 5 K/min) of a preheated (MgFe)-gel in air (a). The *inset* in a shows the corresponding MS signals. TG/DTA curves in argon atmosphere (b)

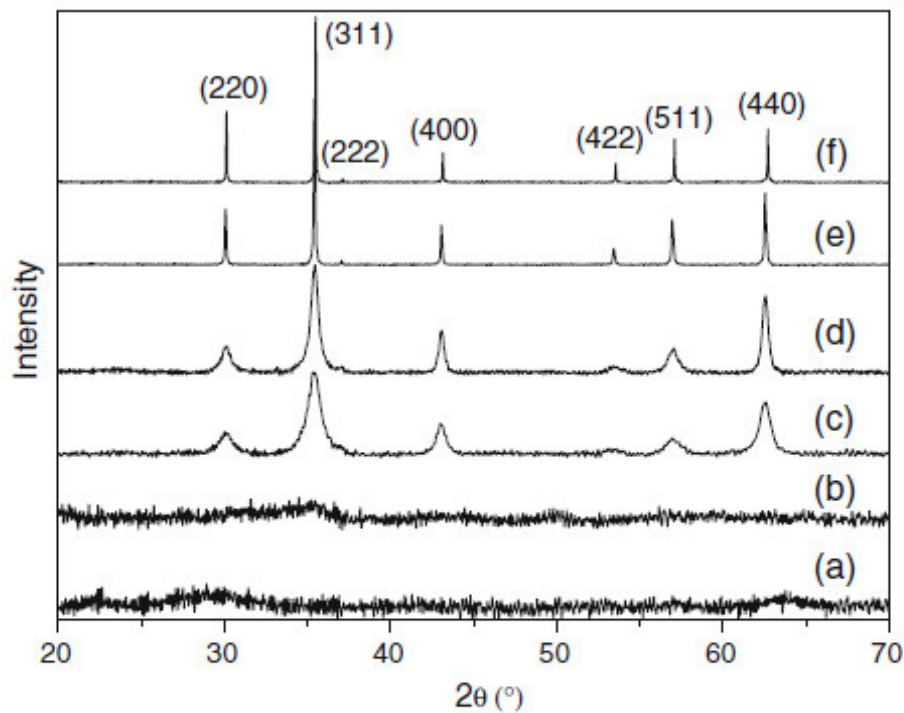


Fig. 2 Room temperature XRD patterns of the (MgFe)-gel (a) and resulting calcination products (b–f) at various temperatures (soaking time 2 h, rate 5 K/min): b 400 °C, c 550 °C (powder 1a), d 700 °C (powder 1c), e 1000 °C (powder 1f). Graph f shows the XRD pattern of powder 2

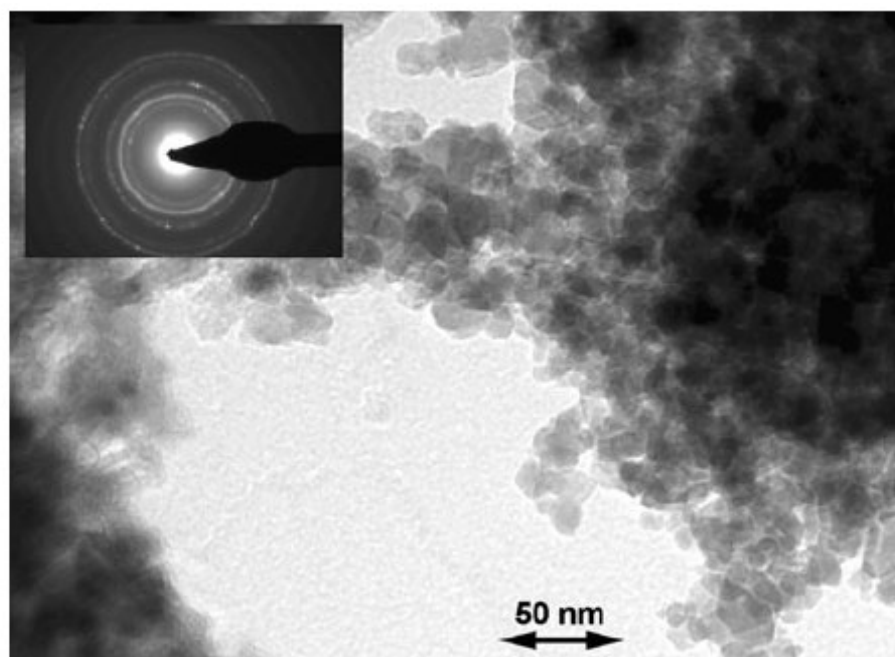


Fig. 3 TEM image of powder 1a

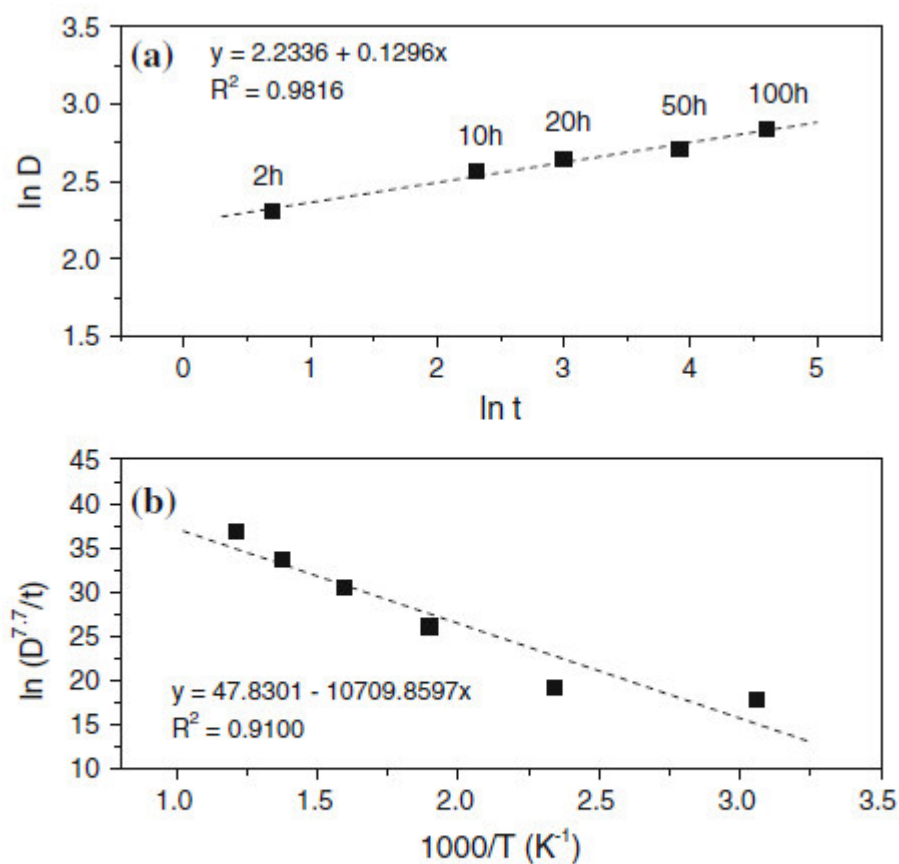


Fig. 4 a $\ln D$ (crystallite size) versus $\ln t$ (calcination time) for MgFe_2O_4 calcined at 600 °C, (b) plot of $\ln(D^{7.7}/t)$ as a function of $1/T$ for samples calcined for 2 h

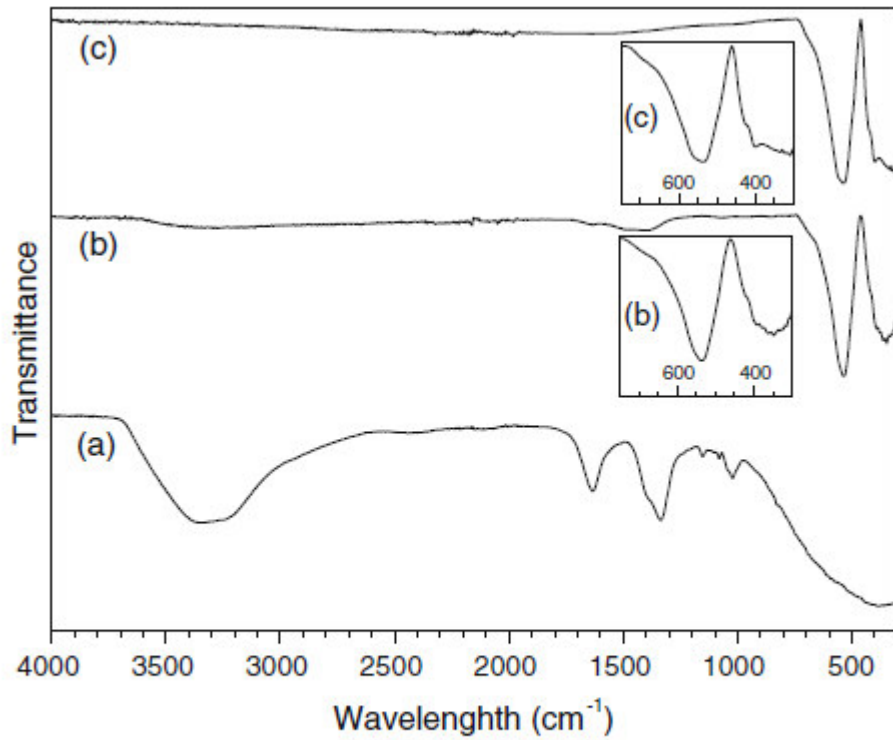


Fig. 5 FT-IR spectra (ATR technique) of (a) (MgFe)-gel, (b) powder 1a and (c) powder 1f

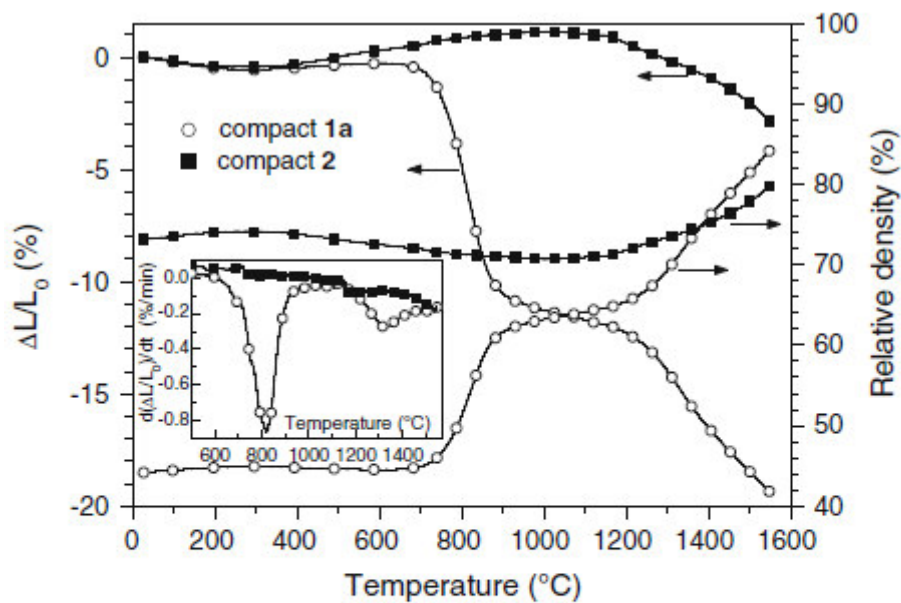


Fig. 6 Non-isothermal dilatometric measurements of green bodies of 1a and 2 in flowing air (heating rate 10 K/min). The relative densities were calculated assuming an isotropic shrinkage behaviour. The inset shows the relative shrinkage rates ($d(\Delta L/L_0)/dt$). The green densities are 2.0 g/cm^3 (1a) and 3.3 g/cm^3 (2), respectively

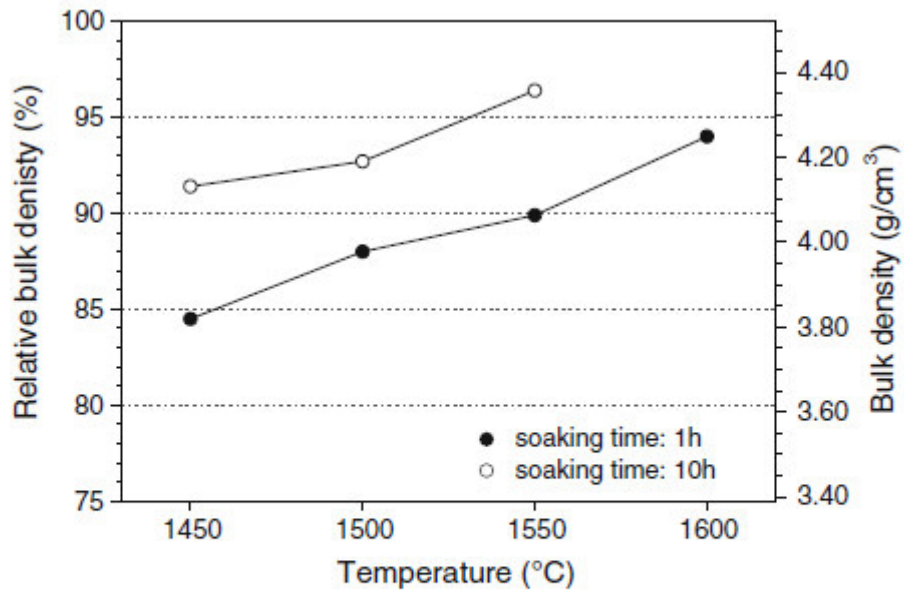


Fig. 7 Final bulk densities versus sintering temperature of ceramic bodies of **1a** (soaking time: 1 and 10 h, heating-/cooling rate: 10 K/min)

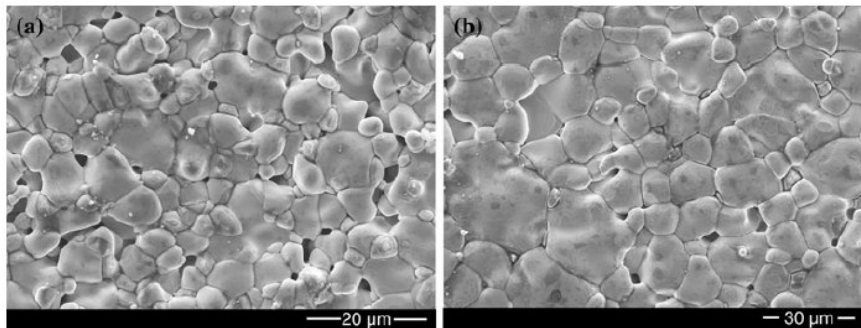


Fig. 8 SEM surface images of ceramic bodies of **1a** after isothermal sintering at 1450 °C (heating-/cooling rate: 10 K/min): a soaking time 1 h and b soaking time 10 h

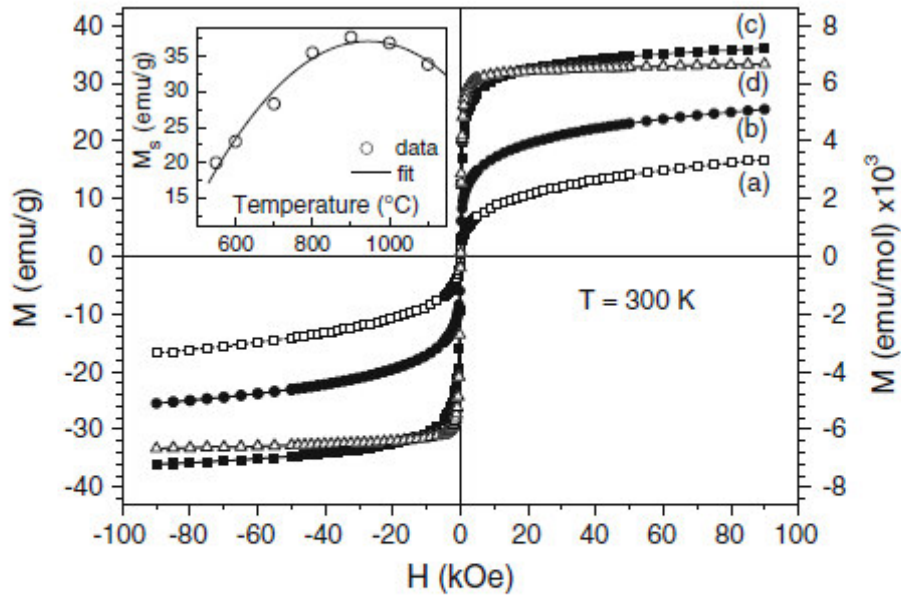


Fig. 9 Magnetization (M) versus applied magnetic field (H) of various MgFe_2O_4 powders at 300 K. *a* Powder 1a, *b* powder 1c, *c* powder 1e and *d* powder 1g. The *inset* shows the saturation magnetization (M_s) depending on calcination temperature

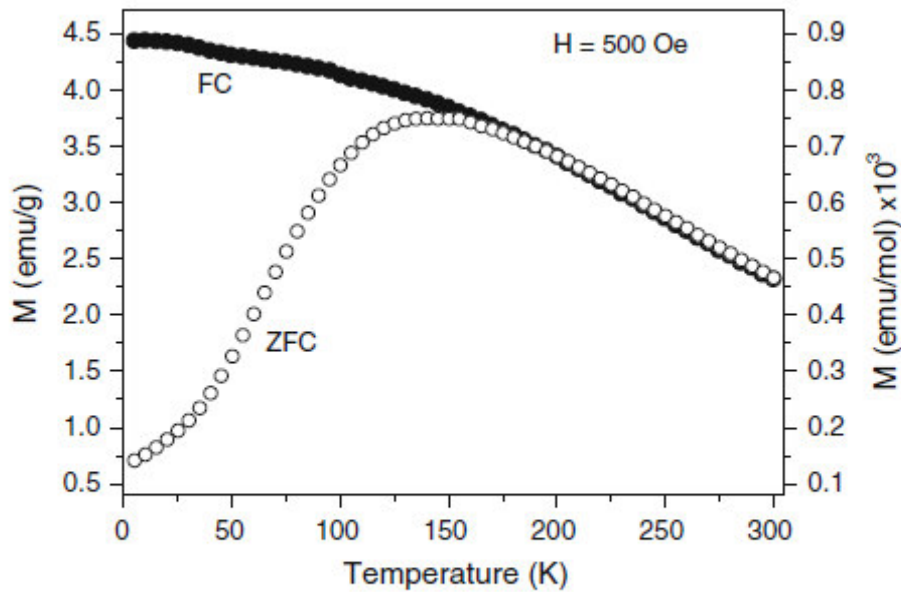


Fig. 10 Temperature dependence of the magnetization for zero-field-cooled (ZFC) and field-cooled (FC) powder 1a in the range 5–300 K

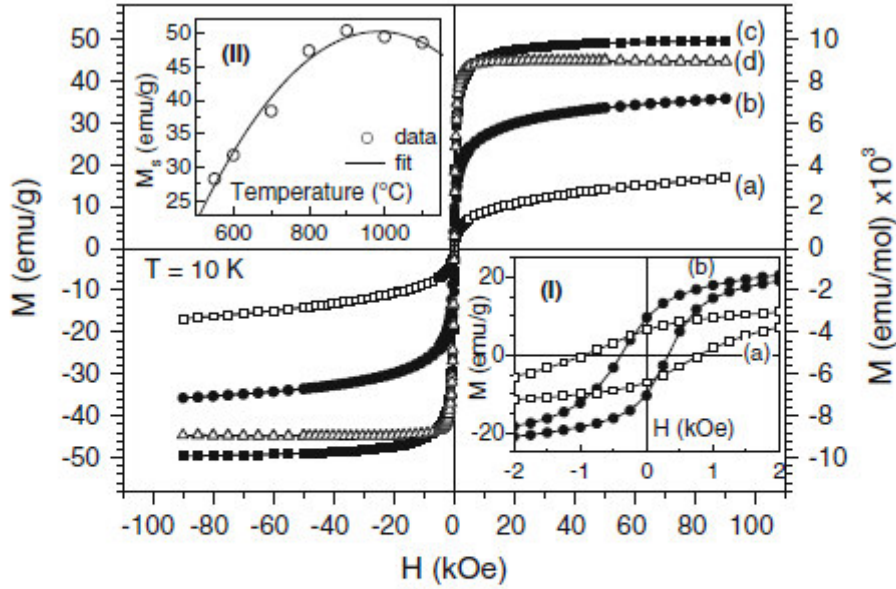


Fig. 11 Magnetization (M) versus applied magnetic field (H) of various MgFe_2O_4 powders at 10 K. *a* Powder 1a, *b* powder 1c, *c* powder 1e and *d* powder 1g. *Inset (I)* shows the saturation magnetization (M_s) depending on calcination temperature and *inset (II)* shows M versus H in a small field range of powders 1a and 1c

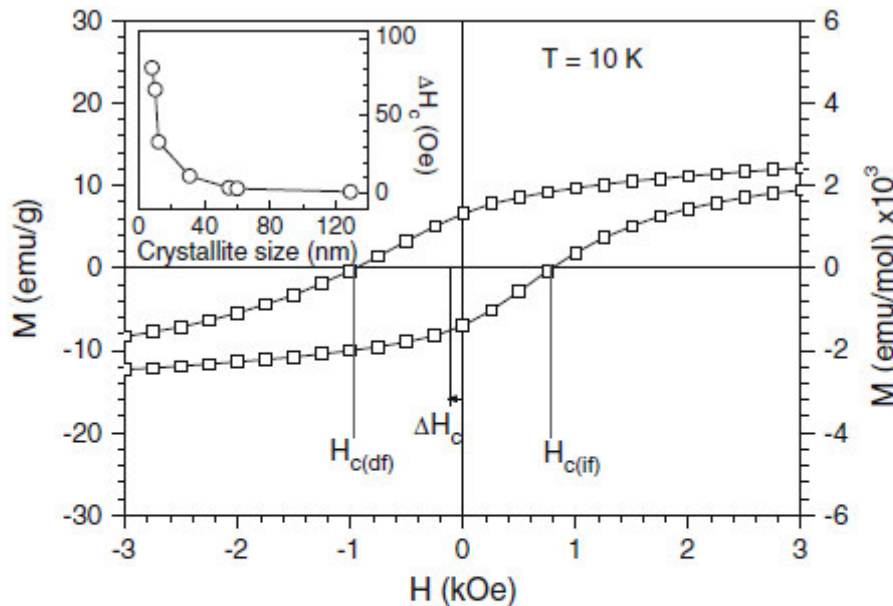


Fig. 12 Magnetization (M) versus applied magnetic field (H) of powder 1a at 10 K in the range of small magnetic fields. The coercivity shift (ΔH_c), the coercivity at decreasing field ($H_{c(df)}$) and the coercivity at increasing field ($H_{c(if)}$) are indicated in the figure. The *inset* shows the coercivity shift (ΔH_c) depending on the crystallite size

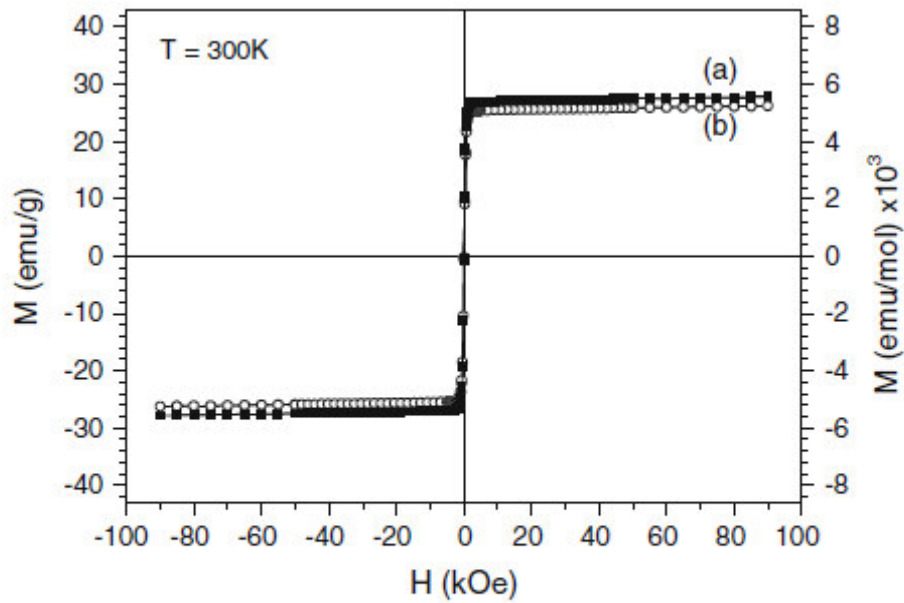


Fig. 13 Magnetization (M) versus applied magnetic field (H) of ceramic bodies from powder 1a at 300 K. *a* Sintering at 1450 °C for 1 h and *b* sintering at 1600 °C for 1 h

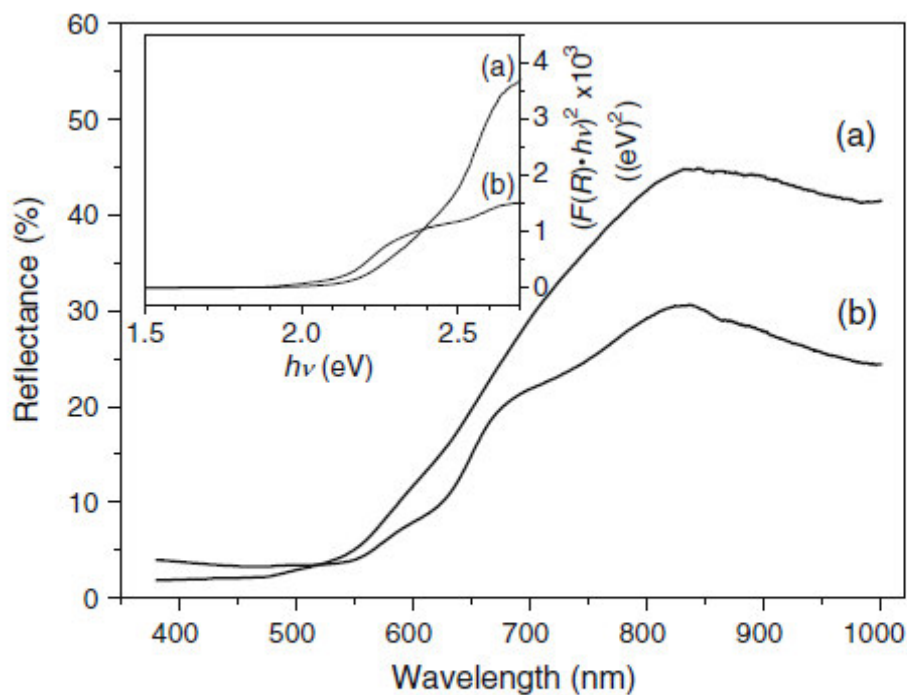


Fig. 14 Diffuse reflectance versus wavelength for powder 1a (*a*) and a corresponding ceramic body sintered at 1450 °C for 1 h (*b*). The inset shows the graphical representation of $(F(R) \cdot hv)^2$ versus hv

References

- [1] Rane KS, Verenkar VMS, Sawant PY (2008) *Bull Mater Sci* 24: 323–330.
- [2] Goldman A (2006) *Modern Ferrite Technology*. Springer Science+Business Media Inc., New York.
- [3] Ma N, Yue Y, Hua W, Gao Z (2003) *Appl Catal A* 251: 39–47.
- [4] Ma X, Sun H, Liu W, Zheng M (2007) *Fresen Environ Bull* 16: 745–748.
- [5] Lee YH, Lee GD, Park SS, Hong SS (2005) *React Kinet Catal Lett* 84: 311–317.
- [6] Dom R, Subasri R, Radha K, Borse PH (2011) *Solid State Commun* 151: 470–473.
- [7] Xiong C, Chen Q, Lu W, Gao H, Lu W, Gao Z (2000) *Catal Lett* 69: 231–236.
- [8] Gusmano G, Montesperelli G, Nunziante P, Traversa E (1993) *J Mater Sci* 28: 6195–6198.
- [9] Liu YL, Liu ZM, Yang Y, Yang HF, Shen GL, Yu RQ (2005) *Sens Actuators B* 107: 600–604.
- [10] Benko FA, Koffyberg EP (1986) *Mater Res Bull* 21: 1183–1988.
- [11] Candeia RA, Souza MAF, Bernardi MIB, Maestrelli SC, Santos IMG, Souza AG, Longo E (2006) *Mater Res Bull* 41: 183–190.
- [12] Kalendová A (2000) *Prog Org Coat* 38: 199–206.
- [13] Mizoe K, Takiguchi T, Arahira F, Ito M (2005) *Toner and Image Forming Method*. US-Pat. 6897001 B2.
- [14] Watanabe Y, Sato K, Yukumi S, Yoshida M, Yamamoto Y, Doi T, Sugishita H, Naohara T, Maehara T, Aono H, Kawachi K (2009) *Bio-Med Mater Eng* 19: 101–110.
- [15] Yukumi S, Watanabe Y, Horiuchi A, Doi T, Sato K, Yoshida M, Maehara T, Aono H, Naohara T, Kawachi K (2008) *Anticancer Res* 28: 69–74.
- [16] Okawa H, Lee JH, Hotta T, Ohara S, Takahashi S, Shibahashi T, Yamamasu Y (2004) *J Power Source* 131: 251–255.

-
- [17] Tadi R, Kim YI, Sarkar D, Kim C, Ryu KS (2011) *J Magn Magn Mater* 323: 564–568.
- [18] O'Neill HStC, Annersten H, Virgo D (1992) *Am Mineral* 77: 725–740.
- [19] Gateshki M, Petkov V, Pradhan SK, Vogt T (2005) *J Appl Cryst* 38: 772–779.
- [20] R.J. Harrison, A. Putnis, *Phys. Chem. Minerals* 26 (1999) 322–332.
- [21] Sepelák V, Bergmann I, Feldhoff A, Litterst FJ, Becker KD, Cadogan JM, Hofmann M, Hoelzel M, Wang JL, Avdeev M, Campbell SJ (2010) *Hyperfine Interact* 198: 67–71.
- [22] Berchmans LJ, Selvan RK, Kumar PNS, Augustin CO (2004) *J Magn Magn Mater* 279: 103–110.
- [23] Chandradass J, Jadhav AH, Kim H (2012) *Appl Surf Sci* 258: 3315–3320.
- [24] Iqbal MJ, Ahmad Z, Melikhov Y, Nlebedim IC (2012) *J Magn Magn Mater* 324: 1088–1094.
- [25] Hoque SM, Hakim MA, Mamun A, Akhter S, Hasan MT, Paul DP, Chattopadhyay K (2011) *Mater Sci Appl* 2: 1564–1571.
- [26] Akhtar MJ, Younas M (2012) *Solid State Sci* 14: 1536–1542.
- [27] Khot VM, Salunkhe AB, Phadatare MR, Pawar SH (2012) *Mater Chem Phys* 132: 782–787.
- [28] Maensiri S, Sangmanee M, Wiengmoon A (2009) *Nanoscale Res Lett* 4: 221–228.
- [29] Kraus W, Nolze G (1998) *Powder Diffr* 13: 256–259.
- [30] Program WinXPOW v1.06 (1999). Stoe & Cie GmbH, Darmstadt.
- [31] Stokes AR, Wilson AJC (1994) *Proc Phys Soc* 56: 174–181.
- [32] Allred VD, Buxton SR, McBride JP (1957) *J Phys Chem* 61: 117–120.
- [33] PDF 2 (International Centre for Diffraction Data, Pennsylvania) (2001). MgFe_2O_4 [71-1232], Fe_2O_3 [72-469], Fe [6-696], FeO [6-615], $\text{Mg}_{1-x}\text{Fe}_x\text{O}$ [35-1393].
- [34] Qian YT, Kershaw R, Dwight K, Wold A (1983) *Mater Res Bull* 18: 543–548.

-
- [35] Buscaglia MT, Bassoli M, Buscaglia V, Alessio R (2005) *J Am Ceram Soc* 88: 2374–2379.
- [36] Cun W, Xinming W, Jincai Z, Bixian M, Guoying S, Ping'an P, Jiamo F (2002) *J Mater Sci* 37: 2989–2996.
- [37] Changa PR, Zheng P, Liu B, Anderson DP, Yu J, Ma X (2011) *J Hazard Mater* 186: 2144–2150.
- [38] Nakamoto K (1986) *Infrared and Raman Spectra of Inorganic and Coordination Compounds*. John Wiley & Sons, USA.
- [39] Fang JM, Fowler PA, Tomkinson J, Hill CAS (2002) *Carbohydr Polym* 47: 245–252.
- [40] Gadkari AB, Shinde TJ, Vasambekar PN (2010) *J Mater Sci Mater Electron* 21: 96–103.
- [41] Josyulu OS and Sobhanadri J (1981) *phys stat sol (a)* 65: 479–483.
- [42] Gaudon M, Pailhe N, Wattiaux A, Demourgues A (2009) *Mater Res Bull* 44: 479–484.
- [43] Köferstein R, Jäger L, Zenkner M, Ebbinghaus SG (2009) *J Eur Ceram Soc* 29: 2317–2324.
- [44] Schatt W (1992) *Sintervorgänge*. VDI-Verlag, Düsseldorf.
- [45] Hirata Y, Hara A, Aksay IA (2009) *Ceram Int* 35: 2667–2674.
- [46] Kirichok PP, Antoshchuk AP (1977) *Izv Akad Nauk Neorg Mater* 13: 1327–1330.
- [47] Phillips B, Somiya S, Muan A (1961) *J Am Ceram Soc* 44: 167–169.
- [48] Ahmed YMZ, Ewais EMM, Zaki ZI (2010) *J Alloy Comp* 489: 269–274.
- [49] Özgür Ü, Alivov Y, Morkoc H (2009) *J Mater Sci Mater Electron* 20: 789–834.
- [50] Chikazumi S (2005) *Physics of Ferromagnetism*. Oxford University Press.
- [51] Krissman CJ, Harrison SE (1956) *Phys Rev* 103: 857–860.
- [52] Antic B, Jovic N, Pavlovic MB, Kremenovic A, Manojlovic D, Vucinic-Vasic M, Nikolic AS (2010) *J Appl Phys* 107: 043525.

-
- [53] Rashad MM (2007) *J Mater Sci* 42: 5248–5255.
- [54] Chen C, Rondinone AJ, Chakoumakos BC, Zhang ZJ (1999) *J Magn Magn Mater* 194: 1–7.
- [55] Chen Q and Zhang ZJ (1998) *Appl Phys Lett* 73: 3156–3158.
- [56] Nogues J and Schuller IK (1999) *J Magn Magn Mater* 192: 203–232.
- [57] Sepelak V, Feldhoff A, Heitjans P, Krumeich F, Menzel D, Litterst FJ, Bergmann I, Becker KD (2006) *Chem Mater* 18: 3057–3067.
- [58] Sepelak V, Baabe D, Mienert D, Litterst FJ, Becker KD (2003) *Scr Mater* 48: 961–966.
- [59] Kodama RH, Makhlof SA, Berkowitz AE (1997) *Phys Rev Lett* 79: 1393–1396.
- [60] Nipan GD, Ketsko VA, Stognij AI, Trukhanov AV, Koltsova TN, Kopeva MA, Elesina LV, Kuznetsov NT (2010) *Inorg Mater* 46: 429–433.
- [61] Kim HG, Borse PH, Jang JS, Jeong ED, Jung OS, Suh YJ, Lee JS (2009) *Chem Commun* 5889–5891.
- [62] Kubelka P, Munk F (1931) *Z. Techn. Phys.* 11: 593–601.
- [63] Kortüm G and Vogel J (1958) *Z Phys Chem* 18: 110–122.
- [64] Nowak M, Kauch B, Szperlich P (2009) *Rev Sci Instrum* 80: 046107.
- [65] McLean TP (1960) In: Gibson AF (ed) *Progress in Semiconductors*, Vol. 5, Heywood, London.
- [66] Roduner E (2006) *Chem Soc Rev* 35: 583–592.